

An Efficient Forecasting Approach for the Real-Time Reduction of Boundary Effects in Time-Frequency Representations

Adrien Meynard, Hau-Tieng Wu

Abstract—Time-frequency (TF) representations of time series are intrinsically subject to the boundary effects. As a result, the structures of signals that are highlighted by the representations are garbled when approaching the boundaries of the TF domain. In this paper, for the purpose of real-time TF information acquisition of nonstationary oscillatory time series, we propose a numerically efficient approach for the reduction of such boundary effects. The solution relies on an extension of the analyzed signal obtained by a forecasting technique. In the case of the study of a class of locally oscillating signals, we provide a theoretical guarantee of the performance of our approach. Following a numerical verification of the algorithmic performance of our approach, we validate it by implementing it on biomedical signals.

Index Terms—Boundary effects, time-frequency, forecasting, nonstationarity

I. INTRODUCTION

IN any digital acquisition system, the study and the interpretation of the measured signals generally require an analysis tool, which enables researchers to point out the useful characteristics of the signal. The need for signal analysis arises from various signals, ranging from audio [1], [2], mechanical [3], or biomedical signals [4]. For instance, biomedical signals, such as photoplethysmogram (PPG), contain several characteristics, including respiratory rate or blood pressure, that cannot be interpreted from its run-sequence plot in the time domain. An analysis tool would make possible the extraction of these useful characteristics.

Usually, the measured signals exhibit nonstationary behavior, and the observed quantities might be interfered by transient phenomena that can vary rapidly and irregularly. In this paper, we focus on oscillatory time series. These signals might, for example, oscillate fast with large amplitude at one moment, and then oscillate slowly with small amplitude at the next moment. In order to adapt the analysis to nonstationarities, local spectral analysis is generally performed [5], [6]. The short-time Fourier transform [7] (STFT), a typical tool built for this purpose, enables the determination of the local frequency content of a nonstationary signal.

Windowing is a common method for performing local analysis. Among many others, STFT [8], continuous wavelet transform (CWT) [9], synchrosqueezing transform (SST) [10], and reassignment [11] (RS) are representations that fall back on the use of an analysis window. Let $x : I \rightarrow \mathbb{R}$ denote the observed signal, where I denotes the finite interval where the signal is measured. Let $g_s : \mathbb{R} \rightarrow \mathbb{R}$ denote the analysis window, where s is a shape parameter. The support of g_s is localized around the origin and is small with respect to $|I|$. The translation operator is T_τ defined as:

$$T_\tau f = f(t - \tau), \quad \forall f : \mathbb{R} \rightarrow \mathbb{R}.$$

Then, the local analysis of x around the instant $\tau \in I$ rely on the evaluation of the following inner product:

$$V_x(s, \tau) = \langle x, T_\tau g_s \rangle_I. \quad (1)$$

A major shortcoming of this technique occurs when analyzing the signal x near the boundaries of the interval I . Clearly, at these points, half of the information is missing. Consequently, the results of the inner product (1) are distorted. This phenomenon is usually understood as the *boundary effect*. We display on the bottom left of Fig. 1 the result of the SST of a PPG (see section IV-B3 for a comprehensive description). The distortion resulting from boundary effects is clearly visible on the right side of this representation. Indeed, while in the major left part of the image, clear lines stand out, they become blurred as they approach the right boundary of the image. Therefore, estimations of signal characteristics, like instantaneous frequencies [12] or amplitudes, from this TF representation appear to be imprecisely determinable (or even likely to fail) in the vicinity of the boundaries. Moreover, this boundary effect would unavoidably limit applying these window-based TF analysis tools for real-time analysis purposes. It is thus desirable to have a solution to eliminating the boundary effects.

Attempts to minimize the boundary effects generally consists in softening the discontinuity on signal edges. For instance, judicious choices of analysis windows whose support does not interfere with the boundary points can minimize the occurrence of aberrant patterns near the boundaries of the TF plane [13], [14]. Due to the specific relationship of chosen analysis windows and TF analysis tool, these techniques do not make it possible to



Figure 1. A segment of PPG signal (top) and the right boundary of a TF representation determined by the SST without extension (bottom left), and the right boundary of a TF representation determined by the SST with the proposed boundary effect reduction algorithm by forecasting (bottom right). The window length for the SST is 12 sec.

reduce the boundary effects of any TF representations, and for any analysis window. Another natural idea consists of carrying out a preliminary step of extending the signal beyond its boundaries, and due to its flexibility, various extension schemes have been proposed. For example, there exist simple extension schemes that do not take into account the dynamical behavior of the signal, such as zero-padding, periodic extension, symmetric extension [15], [16], or polynomial extrapolation [17]. There also exist extension schemes based on physically relevant dynamical models, such as the Extended Dynamic Mode Decomposition [18] (EDMD), the Gaussian process regression [19], [20] (GPR), the Trigonometric, Box-Cox transformation, ARMA errors, Trend and Seasonal components (TBATS) algorithm [21], the dynamic linear models [22], and long short-term memory model [23]. It is a far from an exhaustive list, and we refer readers with interest to [24] for a friendly monograph on the general forecasting topic. While the second class of extension schemes gives better-extended signals than the first class, they generally have a great computational cost.

In this paper, we propose a fast extension algorithm based on a simple dynamical model, in order to optimize the trade-off between the extension quality and the computational cost. The proposed algorithm is then composed of two steps.

- 1) *Extend the signal by forecasting it.* The aim is to use a dynamic model to predict the values taken by the measured signal outside the measurement interval. Then, once this operation is done, we have access to an extended signal defined on a larger interval I_Δ , where Δ denotes the size of the extension on both boundaries of I .

- 2) *Run the local analysis tool on the extended signal.* Assuming that the support of the analysis window is smaller than 2Δ , the local analysis near the boundary of I is now possible without lack of information thanks to knowledge brought by the extension.

Thus, assuming that the quality of the extension step is sufficient, the analysis results obtained that way will be less sensitive to the boundary effects than the result of the analysis tool applied directly to the non-extended signal. We claim and prove that forecasting oscillatory signals based on the simple dynamical model combined with the simple least square approach is sufficient for reducing the boundary effects for the TF analysis, or other kernel-based analysis. See the bottom right of Fig. 1 for a snapshot of the result. The main benefit of this simple approach is a numerically efficient solution with a theoretical guarantee for real-time analysis purposes.

The paper is organized in the following way. In section II, we provide an extension method based on a linear dynamic model. We derive the corresponding algorithm for boundary effects reduction. In section III, we show that the dynamic model we consider is sufficient to extend signals taking the form of sums of sine waves. An evaluation of the theoretical performance of our algorithm on a class of signals, the sums of sine waves, is given in section III. In section IV, we compare our extension method with more sophisticated methods such as EDMD, GPR, or TBATS. We show that our algorithm gives fast results of reasonable quality. Finally, we evaluate the performance of our boundary effects reduction algorithm on biomedical signals, such as respiratory signals, and compare it to the theoretical results.

II. ALGORITHM

As explained above, the algorithm for the reduction of boundary effects on TF representations relies on extending the signal by forecasting it before applying the TF analysis.

We start with the notation. Let $x : \mathbb{R} \rightarrow \mathbb{R}$ denote a continuous-time signal. In this work, we consider a finite-length discretization of that one. Thus, the sampled signal \mathbf{x} , whose length is denoted by N , is such that

$$\mathbf{x}[n] = x\left(\frac{n}{f_s}\right), \quad \forall n \in \{0, \dots, N-1\},$$

where f_s denotes the sampling frequency. Let M and K be two integers such that $M < N$ and $K + M < N$. Then, for all $k \in \{0, \dots, K-1\}$, we extract from $\mathbf{x} \in \mathbb{R}^N$ the sub-signal $\mathbf{x}_k \in \mathbb{R}^M$ given by:

$$\mathbf{x}_k = \begin{pmatrix} \mathbf{x}[N - K + (k-1) - (M-1)] \\ \vdots \\ \mathbf{x}[N - K + (k-1)] \end{pmatrix}. \quad (2)$$

These sub-signals are gathered into the matrix $\mathbf{X} \in \mathbb{R}^{M \times K}$ such that:

$$\mathbf{X} = (\mathbf{x}_0 \quad \dots \quad \mathbf{x}_{K-1}).$$

Notice that these sub-signals are overlapping each other. Indeed, \mathbf{x}_{k+1} is a shifting of \mathbf{x}_k from one sample. We also consider the matrix $\mathbf{Y} \in \mathbb{R}^{M \times K}$ given by:

$$\mathbf{Y} = (\mathbf{x}_1 \quad \cdots \quad \mathbf{x}_K) .$$

The boundary effect reduction algorithm is based on manipulating \mathbf{X} and \mathbf{Y} .

The pseudo-code of the proposed real-time algorithm to reduce boundary effects on windowing-based TF representations is shown in Algorithm 1. We coined the algorithm **BoundEffRed**. Below, we detail the algorithm, particularly the signal extension **SigExt** in Algorithm 2.

Algorithm 1 Tackling boundary effects of a TF representation in real-time. $\mathbf{F}_x = \text{BoundEffRed}(\mathbf{x}, M, K, L, \mathcal{F})$

Inputs: $\mathbf{x}_N, M, K, N_0, L, \mathcal{F}$

while N increases **do**

Real-time input: \mathbf{x}_N

Forecasting step.

- Signal extension: $\tilde{\mathbf{x}}_{N+L} = \text{SigExt}(\mathbf{x}_N)$.

Representation estimation step.

- Extended representation evaluation: $\mathcal{F}(\tilde{\mathbf{x}}_{N+L})$.
- Restriction of $\mathcal{F}(\tilde{\mathbf{x}}_{N+L})$ to the current time interval (see (9)) to obtain $\mathbf{F}_x^{(N)} = \mathcal{F}^{\text{ext}}(\mathbf{x}_N)$.

Real-time output: Signal representation $\mathbf{F}_x^{(N)}$
end while

A. Step 1: Extension by forecasting

a) *Dynamical model and forecasting:* Establishing a dynamical model consists in determining the relation linking \mathbf{Y} to \mathbf{X} , that is finding a function f so that

$$\mathbf{Y} = f(\mathbf{X}) .$$

In a general framework, forecasting means estimating the function f from the observed values taken by the signal, in order to predict its future values. For instance, the dynamic mode decomposition [25], [18] or other more complicated models [20], [21], [22], [23], allow this by setting additional constraints on the behavior of f . We will see, in section III, that considering such a complex dynamic model is not necessary for the study of the oscillatory signals of interest to us. That is why we consider here a naive dynamical model, assuming that we have the following relation:

$$\mathbf{Y} = \mathbf{A}\mathbf{X} , \quad (3)$$

where $\mathbf{A} \in \mathbb{R}^{M \times M}$. In other words, we adopt a classical strategy in the study of dynamical systems, the *linearization* of a nonlinear phenomenon, when the system is sufficiently regular. Notice that this linearized dynamical model can be written equivalently in function of the sub-signals \mathbf{x}_k , as:

$$\mathbf{x}_{k+1} = \mathbf{A}\mathbf{x}_k , \forall k \in \{0, \dots, K-1\} . \quad (4)$$

The forecasting method consists in estimating the unknown matrix \mathbf{A} . Indeed, let $\tilde{\mathbf{A}}$ denotes the estimate of \mathbf{A} . We then obtain the forecasting of the signal at time $\frac{N-1+\ell}{f_s}$ by:

$$\tilde{\mathbf{x}}[N-1+\ell] = \boldsymbol{\alpha}^{(\ell)} \mathbf{x}_K , \quad (5)$$

where $\boldsymbol{\alpha}^{(\ell)}$ denotes the last row of $\tilde{\mathbf{A}}^\ell$; that is to say,

$$\boldsymbol{\alpha}^{(\ell)} = \mathbf{e}_M^T \tilde{\mathbf{A}}^\ell , \quad (6)$$

where \mathbf{e}_M is the unit vector of length M given by $\mathbf{e}_M = (0 \quad \cdots \quad 0 \quad 1)^T$.

b) *Model estimation:* To estimate the matrix \mathbf{A} , we consider the simple but numerically efficient least square estimator. That is, we solve the following problem:

$$\tilde{\mathbf{A}} = \arg \min_{\mathbf{A}} \mathcal{L}(\mathbf{A}) , \quad (7)$$

where the loss function \mathcal{L} is given by:

$$\mathcal{L}(\mathbf{A}) = \|\mathbf{Y} - \mathbf{A}\mathbf{X}\|^2 = \sum_{k=0}^{K-1} \|\mathbf{x}_{k+1} - \mathbf{A}\mathbf{x}_k\|^2 .$$

Therefore, solving the problem (7), i.e. $\nabla \mathcal{L}(\tilde{\mathbf{A}}) = \mathbf{0}$, gives the following estimate $\tilde{\mathbf{A}}$ of the dynamical model matrix \mathbf{A} :

$$\tilde{\mathbf{A}} = \mathbf{Y}\mathbf{X}^T(\mathbf{X}\mathbf{X}^T)^{-1} . \quad (8)$$

Remark 1. This expression clearly shows that the matrix $\tilde{\mathbf{A}}$ takes the following form:

$$\tilde{\mathbf{A}} = \begin{pmatrix} 0 & 1 & 0 & \cdots & 0 \\ \vdots & \ddots & \ddots & \ddots & \vdots \\ \vdots & & \ddots & \ddots & 0 \\ 0 & \cdots & \cdots & 0 & 1 \\ \alpha_1 & \cdots & \cdots & \cdots & \alpha_M \end{pmatrix} .$$

Then, except for the row vector $\boldsymbol{\alpha} = (\alpha_1 \cdots \alpha_M)$, the matrix \mathbf{A} is fully determined by the dynamical model.

c) *Signal extension:* Since we are building a real-time algorithm, we consider that only the right “side” of the signal has to be extended, the left “side” being fixed since it only concerns the past values of the signal. We therefore construct the extended signal $\tilde{\mathbf{x}} \in \mathbb{R}^{N+L}$ concatenating the observed signal \mathbf{x} , and the forward forecasting $\tilde{\mathbf{x}}_{\text{fw}} \in \mathbb{R}^L$. We summarize the extension step in Algorithm 2. Notice that we could, if necessary, handle the backward estimation using the same strategy as described above, but applying it to the reverse signal $\mathbf{x}^r = (\mathbf{x}[N-1] \quad \cdots \quad \mathbf{x}[0])^T$.

B. Step 2: Extended Time-Frequency Representation

Let $\mathcal{F} : \mathbb{R}^N \rightarrow \mathbb{C}^{F \times N}$ generically denotes the TF representation of interest to us, which could be, for instance, STFT, CWT, SST, or RS. Here, F typically denotes the size of the discretization along the frequency axis. Due to the boundary effects, the representation $\mathcal{F}(\mathbf{x}_N)$ shows undesired patterns when approaching its edges.

Algorithm 2 Signal extension. $\tilde{\mathbf{x}} = \text{SigExt}(\mathbf{x}, M, K, L)$

Inputs: \mathbf{x}_N, M, K, L
Forward forecasting.

- Estimation of the matrix $\tilde{\mathbf{A}}$ via equation (8).
- Forecasting $\tilde{\mathbf{x}}_{\text{fw}} \in \mathbb{R}^L$ obtained applying equation (5) with $\ell \in \{1, \dots, L\}$.

Output: Extended signal $\tilde{\mathbf{x}}_{N+L} = (\mathbf{x}_N \quad \tilde{\mathbf{x}}_{\text{fw}})^T$.

To alleviate the boundary effects, we apply the representation to the estimated extended signal $\tilde{\mathbf{x}}$. This strategy moves the boundary effects out of the time interval $I = [0, \frac{N-1}{f_s}]$. Finally, the boundary-effects insensitive representation $\mathcal{F}^{\text{ext}} : \mathbb{R}^N \rightarrow \mathbb{C}^{F \times N}$ of \mathbf{x}_N is given for all $v \in \{0, \dots, F-1\}$, $n \in \{0, \dots, N-1\}$ by:

$$\mathcal{F}^{\text{ext}}(\mathbf{x}_N)[v, n] = \mathcal{F}(\tilde{\mathbf{x}}_{N+L})[v, n]. \quad (9)$$

This amounts to restricting the representation $\mathcal{F}(\tilde{\mathbf{x}}_{N+L})$ to the current measurement interval of \mathbf{x}_N . For the sake of simplicity, we denote the restriction operator by \mathcal{R} , where $\mathcal{R} : \mathbb{C}^{F \times (N+L)} \rightarrow \mathbb{C}^{F \times N}$. Consequently, we have:

$$\mathcal{F}^{\text{ext}}(\mathbf{x}_N) = \mathcal{R}(\mathcal{F}(\tilde{\mathbf{x}}_{N+L})). \quad (10)$$

We call \mathcal{F}^{ext} the *boundary-free TF representation*.

$\mathbf{F}_x^{(N)} \in \mathbb{C}^{F \times N}$ is the estimation of the boundary-free TF representation at iteration N in Algorithm 1. For numerical purposes, and to make the real-time implementation achievable, we do not perform a full re-estimation of \mathcal{F}^{ext} at iteration $N+1$. Instead, the additional knowledge provided by $\mathbf{x}[N+1]$ only influences the values of the last L_{win} columns of $\mathcal{F}^{\text{ext}}(\mathbf{x}_{N+1})$, where L_{win} denotes the window half-length used by the TF representation. Thus, $\mathbf{F}_x^{(N+1)}$ is obtained by the concatenation of the first $N - L_{\text{win}} + 1$ columns of $\mathbf{F}_x^{(N)}$ with the last L_{win} columns of $\mathcal{F}^{\text{ext}}(\mathbf{x}_{N+1})$.

Remark 2. Unlike other representations, RS is not causal and rigorously requires knowing the STFT on the whole time-frequency plane before making any reassignment. Nevertheless, in [26], the authors propose a causal RS that only requires the future values of the STFT within a limited time horizon (typically less than L). We use this version in the paper to enable real-time implementation of RS.

III. THEORETICAL PERFORMANCE

A. Signal model

We model the deterministic part of the observed signal as a multicomponent harmonic signal; that is, a sum of sine waves:

$$\mathbf{z}[n] = \sum_{j=1}^J \Omega_j \cos\left(2\pi f_j \frac{n}{f_s} + \varphi_j\right), \quad (11)$$

where J denotes the number of components, $\Omega_j > 0$ the amplitude of the j -th component, f_j its frequency, and $\varphi_j \in [0, 2\pi)$ its initial phase. For the sake of simplicity,

we make an additional assumption on the frequencies of each component. We assume that for all $j \in \{1, \dots, J\}$:

$$\exists p_j, p'_j \in \mathbb{N}^* : f_j = \frac{p_j}{M} f_s = \frac{p'_j}{K} f_s. \quad (12)$$

In addition, the observed signal is assumed to be corrupted by an additive Gaussian white noise. Therefore, the measured discrete signal \mathbf{x} is written as:

$$\mathbf{x} = \mathbf{z} + \sigma \mathbf{w}, \quad (13)$$

where \mathbf{z} follows model (11), \mathbf{w} is a Gaussian white noise, whose variance is normalized to one. Thus, σ^2 denotes the variance of the additive noise $\sigma \mathbf{w}$.

B. Forecasting error

On the forecasting interval, we decompose the estimated signal $\tilde{\mathbf{x}}$ as follows:

$$\tilde{\mathbf{x}}[n] = \mathbf{z}[n] + \epsilon[n], \quad (14)$$

where ϵ is the forecasting error. When $n \in I = \{0, \dots, N-1\}$, this error contains only the measurement noise, that is $\epsilon[n] = \sigma \mathbf{w}[n]$. Outside the interval I , the importance of the forecasting error ϵ is also affected by the loss of information resulting from the linearization of the dynamical model we consider in (3). To evaluate the actual behavior of the forward forecasting error $\epsilon[n]$ when $n \geq N$, we determine its first two moments.

- 1) The mean, or estimation bias, is such that:

$$\mu[n] \triangleq \mathbb{E}\{\epsilon[n]\} = \mathbb{E}\{\tilde{\mathbf{x}}[n]\} - \mathbf{z}[n].$$

Given the forecasting strategy, we have $\mu[n] = 0$ when $n \in I$ and:

$$\mu[n] = \mathbb{E}\{\alpha^{(\ell)}\} \mathbf{z}_K + \sigma \mathbb{E}\{\alpha^{(n-N+1)} \mathbf{w}_K\} - \mathbf{z}[n] \quad (15)$$

when $n \geq N$.

- 2) The covariance is given by:

$$\begin{aligned} \gamma[n, n'] &\triangleq \mathbb{E}\{(\epsilon[n] - \mu[n])(\epsilon[n'] - \mu[n'])\} \\ &= \mathbb{E}\{\tilde{\mathbf{x}}[n]\tilde{\mathbf{x}}[n']\} - \mathbf{z}[n]\mathbf{z}[n'] - \mu[n]\mathbf{z}[n'] \\ &\quad - \mu[n']\mathbf{z}[n] - \mu[n]\mu[n']. \end{aligned}$$

Thus by definition of the noise, we have $\gamma[n, n'] = \sigma^2 \delta_{n, n'}$ when $(n, n') \in I^2$. When $n \geq N$, let us denote $\ell = n - N + 1$. Then, we have two cases.

- (i) If $n' \in I$:

$$\begin{aligned} \gamma[n, n'] &= \sigma \mathbb{E}\{\mathbf{w}[n'] \alpha^{(\ell)}\} \mathbf{z}_K + \sigma^2 \mathbb{E}\{\mathbf{w}[n'] \alpha^{(\ell)} \mathbf{w}_K\} \\ &\quad - \mathbf{z}[n] \mu[n'] - \mu[n] \mu[n']. \end{aligned} \quad (16)$$

- (ii) If $n' = N - 1 + \lambda \geq N$:

$$\begin{aligned} \gamma[n, n'] &= \mathbf{z}_K^T \mathbb{E}\{\alpha^{(\ell)T} \alpha^{(\lambda)}\} \mathbf{z}_K + \sigma \mathbb{E}\{\alpha^{(\ell)} \mathbf{w}_K \alpha^{(\lambda)}\} \mathbf{z}_K \\ &\quad + \sigma \mathbb{E}\{\alpha^{(\lambda)} \mathbf{w}_K \alpha^{(\ell)}\} \mathbf{z}_K + \sigma^2 \mathbb{E}\{\alpha^{(\ell)} \mathbf{w}_K \alpha^{(\lambda)} \mathbf{w}_K\} \\ &\quad - \mathbf{z}[n] \mathbf{z}[n'] - \mathbf{z}[n] \mu[n'] - \mathbf{z}[n'] \mu[n] - \mu[n] \mu[n']. \end{aligned} \quad (17)$$

Besides, we recall that $\gamma[n, n'] = \gamma[n', n]$.

Expressions (15), (16), and (17) show that these quantities depend on the behavior of the forecasting random vector $\mathbf{a}^{(\ell)}$. In Lemma 1, we specify the asymptotic behavior of the forecasting vector $\mathbf{a}^{(\ell)}$ when the dataset size K is great.

Lemma 1. Let \mathbf{x} be a random vector defined by (13). Let $\mathbf{a}^{(\ell)}$ be the associated forecasting vector for the estimation of $\mathbf{x}[N-1+\ell]$, given by (6) and obtained from the least square estimation (8). Let $\mathbf{a}_0^{(\ell)}$ be the last row of the matrix \mathbf{A}_0^ℓ , where \mathbf{A}_0 is defined by:

$$\mathbf{A}_0 = \left(\frac{1}{K} \mathbf{Z}' \mathbf{Z}^T + \sigma^2 \mathbf{D} \right) \left(\frac{1}{K} \mathbf{Z} \mathbf{Z}^T + \sigma^2 \mathbf{I} \right)^{-1}, \quad (18)$$

where $\mathbf{Z} = (\mathbf{z}_0 \cdots \mathbf{z}_{K-1})$, $\mathbf{Z}' = (\mathbf{z}_1 \cdots \mathbf{z}_K)$, \mathbf{z}_k is the k -th sub-signal extracted from \mathbf{z} in the same way as \mathbf{x}_k is defined from \mathbf{x} in (2), and $\mathbf{D} \in \mathbb{R}^{M \times M}$ is the Toeplitz matrix such that $\mathbf{D}[m, m'] = \delta_{m+1, m'}$.

Let $\mathbf{h}^{(\ell)}$ be the error vector given by:

$$\mathbf{h}^{(\ell)} = \mathbf{a}^{(\ell)} - \mathbf{a}_0^{(\ell)}.$$

Then, the random vector $\mathbf{h}^{(\ell)}$ converges in law to a zero-mean Gaussian random vector when $K \rightarrow \infty$, and we have:

$$\sqrt{K} \mathbf{h}^{(\ell)} \xrightarrow[K \rightarrow \infty]{\mathcal{D}} \mathcal{N} \left(\mathbf{0}, \mathbf{\Gamma}^{(\ell, \ell)} \right), \quad (19)$$

with $\mathbf{\Gamma}^{(\ell, \ell)} = \mathbf{F}^{(\ell)T} \mathbf{\Gamma}_0 \mathbf{F}^{(\ell)}$, where $\mathbf{\Gamma}_0 \in \mathbb{R}^{M(M+1) \times M(M+1)}$ is a covariance matrix and $\mathbf{F}^{(\ell)} \in \mathbb{R}^{M(M+1) \times M}$ is a Jacobian matrix. The expressions of $\mathbf{\Gamma}^{(\ell, \ell)}$ does not depend on K or σ .

Proof. See the Supplementary Material. The proof is based on the multivariate delta method (see paragraph 7.2 in [27]), which gives an asymptotic approximation of a random vector by a Gaussian random vector. ■

Consequently, the covariance between $\sqrt{K} \mathbf{h}^{(\ell)}$ and $\sqrt{K} \mathbf{h}^{(\lambda)}$ remains bounded, i.e.:

$$K \mathbb{E} \left\{ \mathbf{h}^{(\ell)T} \mathbf{h}^{(\lambda)} \right\} \xrightarrow[K \rightarrow \infty]{} \mathbf{\Gamma}^{(\ell, \lambda)} = \mathbf{F}^{(\ell)T} \mathbf{\Gamma}_0 \mathbf{F}^{(\lambda)}.$$

Theorem 1. Let $\mathbf{x} \in \mathbb{R}^N$ be a discrete-time random signal following model (13). Let $\hat{\mathbf{x}}$ denotes its forecasting, obtained using the extension Algorithm 2. Let $n \geq N$ be a sample index. Then, the first-order moment of the forecasting error $\epsilon[n]$ in (14) is approximated by:

$$\mu[n] \underset{K \rightarrow \infty}{\sim} o(\sigma^2) \quad (20)$$

Its second-order moment $\gamma[n, n']$ verify the following approximation equations:

(i) if $n' \in I = \{0, \dots, N-1\}$:

$$\gamma[n, n'] \underset{K \rightarrow \infty}{\sim} \sigma^2 \mathbf{a}_0^{(n-N-1)} [n' - (N-M)] \mathbf{1}_{(n' \geq N-M)} \quad (21)$$

(ii) if $n' \geq N$:

$$\gamma[n, n'] \underset{K \rightarrow \infty}{\sim} \frac{1}{K} \mathbf{z}_K^T \mathbf{\Gamma}^{(\ell, \lambda)} \mathbf{z}_K + \frac{\sigma^2}{K} \text{Tr} \left(\mathbf{\Gamma}^{(\ell, \lambda)} \right) + \sigma^2 \left\langle \mathbf{a}_0^{(\ell)}, \mathbf{a}_0^{(\lambda)} \right\rangle, \quad (22)$$

where $\ell = n - N + 1$ and $\lambda = n' - N + 1$.

Proof. See the Supplementary Material. The proof is mainly based on the results provided by Lemma 1, combined with the Isserlis' theorem [28], which provides a formula for the computation of higher-order moments of Gaussian random variables. ■

Ideally, the forecasting error would behave like the measurement noise $\sigma \mathbf{w}$, i.e. a zero-mean noise whose variance is of the order of σ^2 . Theorem 1 shows that the forecasting error is asymptotically unbiased. Concerning the covariance of the forecasting error, although equations (21) and (22) are not easily readable, one can evaluate the dependence of the variance in function of the tuning parameters, that are adjusted by the user. Let us focus on the forecasting error variance $\gamma[n, n]$ when $n \geq N$. First, as expected, the variance increases linearly with the noise variance σ^2 . Second, it asymptotically depends linearly on the ratio $\frac{1}{K}$. This shows the need to use a sufficiently large dataset to obtain an accurate forecast. Third, the dependency on the sub-signals lengths M and the forecasting index $\ell = n - N + 1$ is hidden in the expression of the covariance matrix $\mathbf{\Gamma}^{(\ell, \ell)}$. We discuss this dependency in more detail in section IV-A1.

Remark 3 (Adaptive Harmonic Model). One can extend the previous result to the case where the instantaneous frequencies and amplitudes of the components of the deterministic part of the observed signal are slowly varying. We therefore handle the AM-FM model which, in its continuous-time version, takes the following form:

$$z(t) = \sum_{j=1}^J a_j(t) \cos(2\pi \phi_j(t)), \quad (23)$$

where a_j and ϕ_j' describe how large and fast the signal oscillate. Clearly, (11) is a special case satisfying the AM-FM model. It is also clear that the forecasting error caused by the SigExt algorithm is additionally sensitive to the speed of variation of the instantaneous amplitudes a_j and frequencies ϕ_j' .

In many practical signals, the amplitude and frequency do not change fast. It is thus reasonable to further restrict the regularity and variations of the instantaneous amplitudes and frequencies of these AM-FM functions so that the signal can be "locally" well approximated by a harmonic function in (11). When these functions satisfy the adaptive harmonic model (AHM) (see [29], [30] for mathematical details) and K is not too large, the signal can be well approximated by (11). Hence, Theorem 1 can still be applied to approximate the error. How to determine the optimal K based on the signal is out of the scope of this paper and will be explored in future work.

C. Performance of the boundary effects reduction

Since it is beyond the scope of the present paper, we do not provide here a generic proof of the reduction of the boundary effects on any TF representation. Instead, let us discuss the particular case of SST. Since SST is designed to analyze signals satisfying the AHM, as is discussed in Remark 3, Theorem 1 ensures that the forecasting error

ϵ defined in (14) is controlled and bounded in terms of mean and covariance. Recall Theorem 3 in [29], which states that when the additive noise is stationary and remains small, the SST of the observed signal remains close to the ideal SST of an AM-FM signal, throughout the TF plane. In our case, while the additive noise is not stationary, the dependence only appears in the extended part of the signal. Thus, the proof of Theorem 3 in [29] can be generalized to explain the robustness of SST to the noise. We refer the reader to [29] for precise quantification of the error made in the TF plane, which depends notably on the covariance of the additive noise and on the speed of variation of the amplitudes and instantaneous frequencies composing the signal. Therefore, in our case, this means that boundary effects are strongly reduced since the forecasting error does not impact SST. An immediate application is that the instantaneous frequencies can now be well estimated continuously up to the edges of the TF plane. While we do not provide a theoretical justification, we verify experimentally that Algorithm 1 is efficient for a large number of representations in the following section IV.

IV. NUMERICAL RESULTS

For the reproducibility purpose, the MATLAB code and datasets used to produce the numerical results in this section are available online at <https://github.com/AdMeynard/BoundaryEffectsReduction>.

A. Evaluation of the forecasting performance

In that section, we first evaluate the quality of the forecasting step and compare it to the theoretical results provided by Theorem 1. The level of the forecasting error depends on at least two parameters:

- The noise variance σ^2 .
- The size of the training dataset K .

In subsections IV-A1 and IV-A2, we study the influence of these parameters. A comparison with the theoretical results of section III is also available.

1) *Sum of sine waves*: We proved that the linear dynamic model is sufficient to catch the dynamical behavior of signals taking the form (11). In order to validate this theoretical result, we apply the forecasting Algorithm 2 to a large number of realizations of the random vector \mathbf{x} of size $N = 10^4$, following model (13), and such that the deterministic component \mathbf{z} takes the form:

$$\mathbf{z}[n] = \cos\left(2\pi p_1 \frac{n}{M}\right) + R \cos\left(2\pi p_2 \frac{n}{M}\right), \quad \forall n \in \{1, \dots, N\},$$

with $M = 150$, $p_1 = 10$, $p_2 = 33$ and $R = 1.4$. Besides, the additive noise is chosen to be Gaussian: $\mathbf{w} \sim \mathcal{N}(\mathbf{0}, \mathbf{I})$.

a) *Influence of the noise variance σ^2* : Here, the size of the training dataset is set to $K = 450$. Then, the forecasting algorithm is run on 1000 realizations of the discrete signal \mathbf{x} for three different values of σ , logarithmically equispaced from 10^{-3} to 10^{-1} . For each of these values, we determine the experimental bias, denoted as

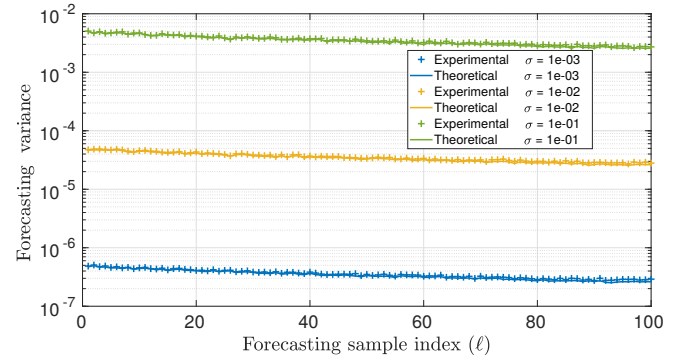


Figure 2. Evolution of the experimental and theoretical forecasting variance in function of the forecasting sample index for different values of σ .

$\mu_{\text{xp}}[N - 1 + \ell]$, and experimental variance, denoted as $\gamma_{\text{xp}}[N - 1 + \ell, N - 1 + \ell]$, in function of the forecasting sample index ℓ (going from 1 to $L = 100$).

The experimental results show that the bias is neither depending on the noise variance σ^2 nor the forecasting length ℓ . Indeed, independently of σ , we always have $\mu_{\text{xp}}[N - 1 + \ell] \in [-0.03\sigma, 0.03\sigma]$, which is negligible with respect to the magnitude of \mathbf{z} . This result confirms the theoretical result (20). In Fig. 2, we display the experimental variance $\gamma_{\text{xp}}[N - 1 + \ell, N - 1 + \ell]$ for each value of σ . The associated theoretical asymptotic forecasting variance (22) is also displayed in solid line. As expected, this result highlights the fact that the forecasting variance increases linearly with respect to σ^2 . The slight decrease of the forecasting variance with ℓ is characteristic of the stationarity of the forecast signal. This shows that as ℓ increases, the prediction becomes less correlated with the measurement noise.

b) *Influence of the training dataset size K* : Here, the noise variance σ is set to $\sigma = 10^{-2}$. Then, the forecasting algorithm is run on 3000 realizations on the discrete signal \mathbf{x} for three different values of K , logarithmically equispaced from 4.5×10^2 to 2×10^3 . For each of these values, we determine the experimental bias $\mu_{\text{xp}}[N - 1 + \ell]$ and variance $\gamma_{\text{xp}}[N - 1 + \ell, N - 1 + \ell]$ in function of the forecasting sample index ℓ (going from 1 to 500).

As in the previous study, the experimental bias vanishes when K increases, confirming the approximation result (20). Besides, the experimental variance is displayed on Fig. 3, and compared with the associated theoretical variance (22). Each color corresponds to these experimental results obtained for a given value of K . This result validates the asymptotic behavior provided by (22), and we can show that the second-order moment $\gamma[\ell, \ell]$ is less dependent on K when K is large.

c) *Summary*: Both previous experimental results combined with the theoretical asymptotic equation (22) allow us to describe the influence of the noise variance and the size of the training dataset on the variance of the forecasting noise, empirically summarized as follows:

$$\gamma[N - 1 + \ell, N - 1 + \ell] \underset{K \rightarrow \infty}{\approx} \frac{\sigma^2}{K} g[\ell]. \quad (24)$$

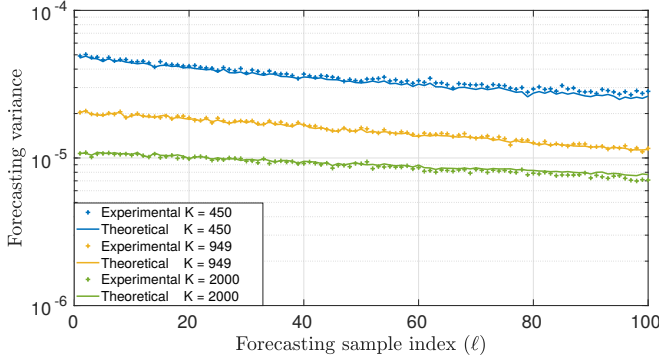


Figure 3. Evolution of the experimental and theoretical forecasting variance in function of the forecasting sample index for different values of K .

where g is a bounded positive function. The empirical result is coherent with the theoretical result provided by Theorem 1.

This study neglects the analysis of the influence of the parameter M , whose influence on the value of the experimental variance is numerically not significant as long as $M \ll 2K$. The choice of this parameter is especially crucial when the deterministic component of the signal is no longer stationary. The AHM, discussed below, is an example.

2) *Adaptive harmonic model*: We now consider a signal satisfying the AHM so that the instantaneous frequencies and amplitudes of its components vary from time to time. The deterministic component \mathbf{z} of the random vector \mathbf{x} (constructed following the model (13)) takes the following form, for all $n \in \{1, \dots, N\}$:

$$\mathbf{x}[n] = \cos(2\pi\phi_1[n]) + R[n] \cos(2\pi\phi_2[n]),$$

where the instantaneous amplitude R is given by:

$$R[n] = 1.4 + 0.2 \cos\left(4\pi \frac{n}{N}\right),$$

and the instantaneous phases are such that:

$$\begin{aligned} \phi_1[n] &= \frac{p_1}{M} \left(n + \frac{0.01}{2\pi} \cos\left(2\pi \frac{n}{N}\right) \right) \\ \phi_2[n] &= p_2 \frac{n}{M} + \frac{20}{2Nf_s} n^2 \end{aligned}$$

Besides, the noise is chosen to be Gaussian: $\mathbf{w} \sim \mathcal{N}(\mathbf{0}, \mathbf{I})$, and we take: $N = 10^4$, $M = 750$, $p_1 = 10$, $p_2 = 23$.

To highlight the fact that the linear dynamical model is sufficient to catch most of the dynamical behavior of signals following the AHM, we compare the performance of Algorithm 1 with a simple extension obtained by pointwise symmetrization [15]. We also evaluate the performance of reference forecasting algorithms that could be used for extending such signals. These methods are:

- The EDMD has been developed by Williams *et al.* [18]. The proposed algorithm is a way to obtain an approximation of the so-called Koopman operator of the observed system, which theoretically allows catching dynamic of nonlinear systems [31].

Table I
AHM SIGNAL: PERFORMANCE OF THE EXTENSION METHODS.

Extension method	MSE		Computing time (sec.)
	Mean	Standard deviation	
SigExt	1.433×10^{-3}	4.361×10^{-4}	0.152
Symmetric	1.019×10^1	1.192×10^2	0.002
EDMD	3.076×10^{-2}	8.095×10^{-2}	2.537
GPR	1.436×10^{-3}	4.346×10^{-4}	146.331
TBATS	1.732×10^{-3}	4.924×10^{-4}	1837.120

- The GPR [19] is a method relying on a probabilistic dynamical model. That one is based on the Gaussian process structure, and therefore offers more flexibility in the type of dynamic that could be modeled than the linear model (3).
- The TBATS method [21] is based on a classical decomposition of times series into a trend, seasonal and ARMA components, with a specific dynamic for the seasonal component. This model demands the estimation of numerous parameters and, by implication, may be slow.

To quantify the global quality (i.e. not depending on ℓ) of the forecasting approaches, we evaluate the Experimental Mean Square Error $\text{MSE}_{\text{xp}}(\tilde{\mathbf{x}})$ of the forward forecast extended signals, namely:

$$\begin{aligned} \text{MSE}_{\text{xp}}(\tilde{\mathbf{x}}) &= \frac{1}{L} \|\tilde{\mathbf{x}} - \mathbf{x}^{\text{ext}}\|^2 \\ &= \frac{1}{L} \sum_{\ell=1}^L \mu_{\text{xp}}[N-1+\ell]^2 + \gamma_{\text{xp}}[N-1+\ell, N-1+\ell]. \end{aligned} \quad (25)$$

where \mathbf{x}^{ext} is the ground-truth extended signal, that is: $\mathbf{x}^{\text{ext}} = (\mathbf{x}[-L] \ \dots \ \mathbf{x}[N-1+L])$. Then, as long as the bias $\mu[N-1+\ell]$ and the variance $\gamma[N-1+\ell, N-1+\ell]$ of the forecasting estimator remain small for all ℓ , the MSE takes small values either. Corresponding results are given in Table I. They show that the naive extension we propose gives satisfying results, in particular in comparison with the point-symmetric extension. Besides, even though the other more sophisticated methods, like GPR, give MSE values that have a slightly smaller standard deviation, these methods are substantially limited by the computing time they require, which prevents them from being used to exploit real-time data. Thus, SigExt is the extension method that optimizes the trade-off between forecasting quality and computing time.

B. Evaluation of the quality of the boundary effects reduction

1) *Metrics*: The quality of the boundary effects reduction is evaluated directly on the TF representation. To that aim, we compare the obtained representation to the optimal representation $\mathcal{F}_N^{\text{opt}}(\mathbf{x})$, defined as the restriction of the representation of the ground-truth extended signal \mathbf{x}^{ext} . Therefore, we have:

$$\mathcal{F}^{\text{opt}}(\mathbf{x}_N) = \mathcal{R}(\mathcal{F}(\mathbf{x}^{\text{ext}})). \quad (26)$$

In the aim of comparing the different techniques, we use a criterion, proposed in [30], that quantifies the

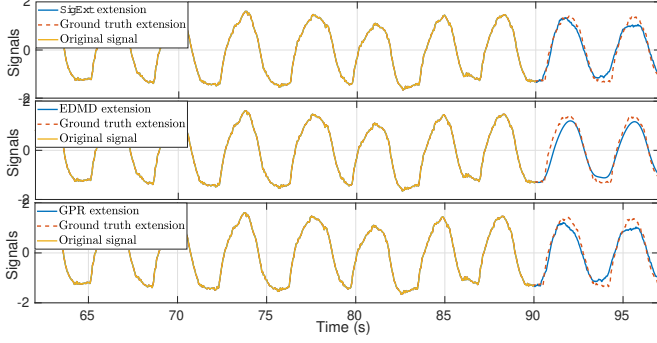


Figure 4. Extended THO signal (blue) obtained by the SigExt forecasting (top), the EDMD forecasting (middle), and the GPR forecasting (bottom), superimposed with the ground truth signal (red dash).

distance between a given TF representation and the optimal one. It is built in analogy with the optimal transport distance, which enables quantifying the distance between two probability density functions. Let us generically denote a time-frequency representation \mathcal{Q} . Then, for t fixed, we consider the following probability density function: $p_{\mathcal{Q}}^t(\xi) = |\mathcal{Q}(\xi, t)|^2 / \int_{\mathbb{R}} |\mathcal{Q}(\nu, t)|^2 d\nu$. At each instant t , we then determine the optimal transport distance d_t between the two densities. It is given by the L^1 norm of the difference between the associated distribution functions. In other words, we have:

$$d_t(\mathcal{Q}, \mathcal{F}_0) = \int_{\mathbb{R}} \left| \tilde{P}_{\mathcal{Q}}^t(\xi) - P_{\mathcal{F}_0}^t(\xi) \right| d\xi,$$

where $P_{\mathcal{Q}}^t(\xi) = \int_{-\infty}^{\xi} p_{\mathcal{Q}}^t(\nu) d\nu$ and $\tilde{P}_{\mathcal{F}_0}^t(\xi) = \int_{-\infty}^{\xi} \tilde{p}_{\mathcal{F}_0}^t(\nu) d\nu$. The *Optimal Transport Distance (OTD)* quantifies the proximity between the estimated and actual instantaneous frequencies while favoring the sparsity of the estimated TF representation. That is why, the performance index $D(\mathcal{Q})$ for the reduction of boundary effects of a given TF representation \mathcal{Q} is given by the ratio between its averaged OTD to the optimal TF representation \mathcal{F}^{opt} (see (26)) and the averaged OTD of the original TF representation \mathcal{F} to \mathcal{F}^{opt} , that is:

$$D(\mathcal{Q}) = \frac{\int_I d_t(\mathcal{Q}, \mathcal{F}^{\text{opt}}) dt}{\int_I d_t(\mathcal{F}, \mathcal{F}^{\text{opt}}) dt}. \quad (27)$$

Thus, $D(\mathcal{Q}) < 1$ means a reduction of the boundary effects. Let us evaluate the quality of the boundary effects reduction on biomedical signals.

2) *Respiratory signal*: We first consider a respiratory signal of 6 hours 20 minutes. This signal, a small portion of which is displayed in Fig. 4, is sampled at $f_s = 100$ Hz.

From that long signal, we build a dataset of 378 non-overlapping signals of 60 seconds, i.e. $N = 6000$. On each of these pieces of signal, we implement the forecasting method introduced in section IV-A2, including the SigExt method detailed in Algorithm 2. However, the TBATS extension method is not implemented here because of its excessive computing time. We forecast 7-second-long extensions on each segment of the signal,

Table II
RESPIRATORY SIGNAL: PERFORMANCE OF EXTENSION METHODS AND ASSOCIATED BOUNDARY-FREE TF REPRESENTATIONS.

Extension method	Averaged MSE	Averaged performance index D			
		STFT	SST	RS	ConceFT
SigExt	0.046	0.698	0.705	0.694	0.776
Symmetric	0.039	0.984	1.280	9.063	1.295
EDMD	0.022	0.635	0.757	0.701	0.793
GPR	0.045	0.793	0.817	0.727	0.876

corresponding to $L = 700$. Thus, in order to catch slowly varying dynamical behaviors, the size of the training signal M is chosen so that $M = \lfloor 1.5L \rfloor$. As a result of section IV-A1, we take: $K = \lfloor 2.5M \rfloor$. The resulting MSE (25) averaged with respect to the simulations are given in Table II. The MSE of SigExt is higher than the MSE of the other methods. This is mainly caused by the presence of a few segments of the whole signal involving complicated behaviors, that are unpredictable via a too simple dynamical model like (3). The left of Fig. 5 illustrates one of those cases, where SigExt fails to catch the fast varying dynamic of the instantaneous amplitude to satisfactorily forecast the signal. The EDMD and Symmetric extensions are more robust to those situations, as shown in this example, and in Table II. Nevertheless, SigExt provides a sufficiently relevant extension to give TF representations sparingly affected by boundary effects. On the right of Fig. 5, we display a comparison between the right boundary of SST of the same segment of signal (top-right), and its boundary-free SST obtained after the SigExt forecasting (bottom-right). The extension of the instantaneous frequency visible on the right side of the image illustrates the reduction of boundary effects produced despite an inaccurate signal forecasting.

We then apply BoundEffRed (i.e. Algorithm 1) for diverse TF representations: STFT, SST, RS, as well as *Concentration of Frequency and Time* (ConceFT), a generalized multitaper SST-based representation introduced in [30]. In this application and throughout the document, we use a Gaussian window as the analysis window, regardless of the representation involved. In Table II, we give the averaged performance index (27), evaluated the whole TF representations (including boundaries). Even though SigExt performs somehow moderately, the boundary effects are dramatically reduced on the TF representations, in the same order of magnitude than with the forecastings given by EDMD or GPR. Notice that the extension length L has been set accordingly to the window length used by the TF analysis tool. For instance, the window length used to evaluate the STFT is of 1500 samples. To prevent the STFT from being sensitive to the boundaries, we set $L = 750$. In this way, the evaluation of the spectral content of the signal near its boundaries is not limited by a lack of information all along the window support. From now on, all results are given for L equal to the half of the width of the window used in the TF transform.

Finally, in order to verify the ability of BoundEffRed

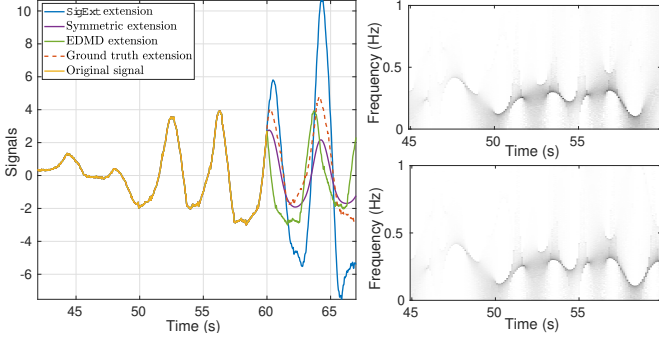


Figure 5. Extensions of a segment of the respiratory signal (left) where SigExt is outperformed by the EDMD and Symmetric extensions. Corresponding SST (top-right) and boundary-free SST obtained with SigExt (bottom-right).

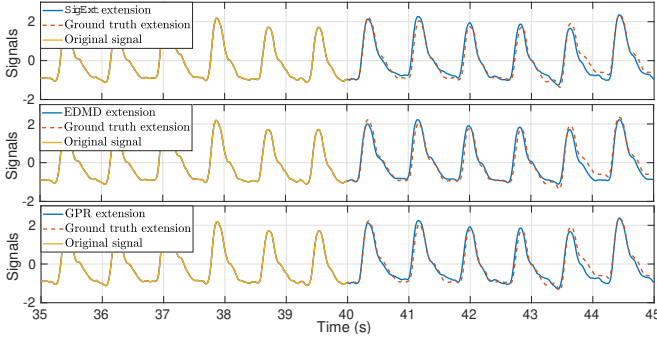


Figure 6. Extended PPG signal (blue) obtained by the SigExt forecasting (top), the EDMD forecasting (middle), and the GPR forecasting (bottom), superimposed with the ground truth signal (red dash).

to be implemented in real time, we evaluate the computation time required for each iteration of Algorithm 1, updating of the boundary-free TF representation. This check is first performed on the real-time SST of a 10-minute sample of the respiratory signal. As the SST is temporally sub-sampled by a ratio of 20, the update should not exceed $20/f_s = 0.2$ sec. This is indeed the case, as no iteration lasted longer than 0.17 sec on a 6-Core Xeon CPU running at 3.5 GHz and 64 GB of RAM.

3) *Photoplethysmogram*: We perform a study similar to the previous one on a 640 second-long photoplethysmogram (PPG) signal extracted from the Physionet dataset [32], [33], sampled at $f_s = 125$ Hz. A portion of this signal is displayed in Fig. 6. The estimated 5 seconds extensions of this segment obtained by SigExt, EDMD, and GPR forecastings are superimposed to the ground-truth extension in Fig. 6.

We divide the signal into 32-second-long segments and apply Algorithm 1 on each piece. We provide in Table III the performance index D of the boundary-free TF representations averaged over the signals. For all the considered TF representations, the results clearly show that our algorithm reduces the boundary effects. Even though on this signal, the SigExt extension yields TF representations slightly more sensitive to boundary effects than the extensions given by EDMD or GPR, it is the only technique that allows a real-time implementation.

Table III
PPG SIGNAL: PERFORMANCE OF THE BOUNDARY-FREE TF REPRESENTATIONS ACCORDING TO THE EXTENSION METHOD.

Extension method	Averaged performance index D		
	STFT	SST	ConceFT
SigExt	0.425	0.713	0.687
Symmetric	1.335	1.340	1.258
EDMD	0.406	0.642	0.615
GPR	0.448	0.766	0.730

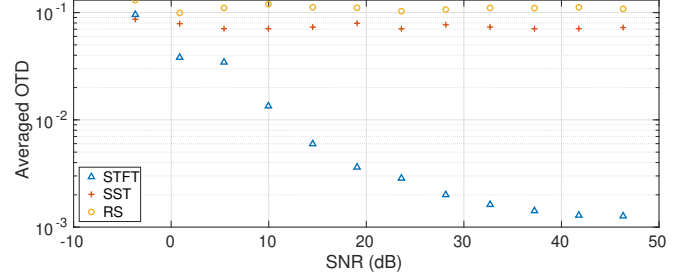


Figure 7. PPG signal. Averaged OTD of BoundEffRed in function of the SNR.

On the bottom-right panel of Fig. 1, we display the SST resulting from the BoundEffRed strategy, applied to the portion of PPG displayed in Fig. 6. We distinctly observe an improvement in the quality of the SST near boundaries. Indeed, the blurring visible when zooming on the right boundary of the SST has almost vanished. The real-time tracking of the instantaneous frequencies contained in the measured signal is therefore largely facilitated.

To evaluate the influence of the noise level on the performance of BoundEffRed, we artificially add Gaussian noise to the measured PPG signal. It is thus an additional noise to the measurement noise actually contained in the signal. Fig. 7 shows the averaged OTD of BoundEffRed for different values of the Signal to Noise Ratio (SNR). We notice that STFT is slightly more sensitive to noise than SST or RS, and STFT performs the best when the added noise is small, i.e. when the SNR is great.

V. CONCLUSION

In this paper, we propose an algorithm, named BoundEffRed, for the real-time reduction of boundary effects in TF representations. This method is based on an extension of the signal obtained by a simple-minded and numerically efficient forecasting. We have shown theoretically that the chosen dynamic model is sufficient to extend signals formed by a sum of sine waves. Moreover, thanks to the low computational time, the numerical results show that this strategy allows us to switch to a real-time implementation of BoundEffRed, unlike other existing forecasting methods. The numerical results also confirmed the robustness to noise of BoundEffRed, as well as its ability to be applied to many time-frequency representations.

Various improvements can be considered to make the algorithm more robust. In particular, we have noticed

(see Fig. 5) that when the regular oscillations of the observed signal break, the forecasting step is no longer relevant, and only slows down the calculation of the TF representation. A preliminary step should then be added to the algorithm to detect signal activity, and disable the forecasting step when possible. A more fundamental improvement would be to perform the forecasting step directly in the TF plane, to specifically predict the evolution of each instantaneous frequency. This would lead to seeing a TF representation as a multivariate time series (corresponding to each frequency band). We will explore these possibilities in our future work.

REFERENCES

- [1] D. Stowell, *Computational Analysis of Sound Scenes and Events*. Springer, 2018, ch. Computational Bioacoustic Scene Analysis, pp. 303–333.
- [2] M. Müller, D. P. W. Ellis, A. Klapuri, and G. Richard, “Signal processing for music analysis,” *IEEE Journal of Selected Topics in Signal Processing*, vol. 5, no. 6, pp. 1088–1110, 2011.
- [3] Z. Peng, F. Chu, and Y. He, “Vibration signal analysis and feature extraction based on reassigned wavelet scalogram,” *Journal of Sound and Vibration*, vol. 253, no. 5, pp. 1087 – 1100, 2002. [Online]. Available: <http://www.sciencedirect.com/science/article/pii/S0022460X01940854>
- [4] M. Akay, *Detection and Estimation Methods for Biomedical Signals*, 1st ed. USA: Academic Press, Inc., 1996.
- [5] P. Stoica and R. Moses, *Spectral analysis of signals*. Upper Saddle River, N.J.: Pearson/Prentice Hall, 2005.
- [6] G. Matz, F. Hlawatsch, and W. Kozek, “Generalized evolutionary spectral analysis and the Weyl spectrum of nonstationary random processes,” *IEEE Transactions on Signal Processing*, vol. 45, no. 6, pp. 1520–1534, Jun. 1997.
- [7] K. Gröchenig, *Foundations of time-frequency analysis*, ser. Applied and Numerical Harmonic Analysis. Boston, MA: Birkhäuser Inc., 2001.
- [8] P. Flandrin, *Time-frequency/time-scale analysis*, ser. Wavelet Analysis and its Applications. San Diego: Academic Press Inc., 1999, vol. 10.
- [9] I. Daubechies, *Ten lectures on wavelets*, ser. CBMS-NSF Regional Conference Series in Applied Mathematics. Philadelphia, PA: Society for Industrial and Applied Mathematics (SIAM), 1992, vol. 61.
- [10] I. Daubechies, J. Lu, and H.-T. Wu, “Synchrosqueezed wavelet transforms: An empirical mode decomposition-like tool,” *Applied and Computational Harmonic Analysis*, vol. 30, no. 2, pp. 243 – 261, 2011. [Online]. Available: <http://www.sciencedirect.com/science/article/pii/S1063520310001016>
- [11] F. Auger, P. Flandrin, Y.-T. Lin, S. McLaughlin, S. Meignen, T. Oberlin, and H.-T. Wu, “Time-frequency reassignment and synchrosqueezing: An overview,” *IEEE Signal Processing Magazine*, vol. 30, no. 6, pp. 32–41, 2013.
- [12] N. Delprat, B. Escudé, P. Guillemain, R. Kronland-Martinet, P. Tchamitchian, and B. Torrèsani, “Asymptotic wavelet and Gabor analysis: extraction of instantaneous frequencies,” *IEEE Transactions on Information Theory*, vol. 38, no. 2, pp. 644–664, Mar. 1992.
- [13] C. K. Chui and E. Quak, *Numerical Methods in Approximation Theory*, ser. ISNM 105: International Series of Numerical Mathematics. Basel: Birkhäuser, 1992, vol. 9, ch. Wavelets on a Bounded Interval, pp. 53–75.
- [14] U. Depczynski, K. Jetter, K. Molt, and A. Niemöller, “The fast wavelet transform on compact intervals as a tool in chemometrics: II. Boundary effects, denoising and compression,” *Chemometrics and Intelligent Laboratory Systems*, vol. 49, no. 2, pp. 151 – 161, 1999. [Online]. Available: <http://www.sciencedirect.com/science/article/pii/S0169743999000374>
- [15] I. Kharitonenko, X. Zhang, and S. Twelves, “A wavelet transform with point-symmetric extension at tile boundaries,” *IEEE Transactions on Image Processing*, vol. 11, no. 12, pp. 1357–1364, 2002.
- [16] L. Chen, T. Q. Nguyen, and K.-P. Chan, “Symmetric extension methods for m-channel linear-phase perfect-reconstruction filter banks,” *IEEE Transactions on Signal Processing*, vol. 43, no. 11, pp. 2505–2511, 1995.
- [17] J. R. Williams and K. Amaratunga, “A discrete wavelet transform without edge effects using wavelet extrapolation,” *The Journal of Fourier Analysis and Applications*, vol. 3, pp. 435–449, 1997.
- [18] M. O. Williams, I. G. Kevrekidis, and C. W. Rowley, “A Data-Driven Approximation of the Koopman Operator: Extending Dynamic Mode Decomposition,” *Journal of Nonlinear Science*, vol. 25, pp. 1307–1346, 2015.
- [19] C. E. Rasmussen and C. K. I. Williams, *Gaussian Processes for Machine Learning*, ser. Adaptive Computation and Machine Learning series. The MIT Press, 2006.
- [20] S. Roberts, M. Osborne, M. Ebden, S. Reece, N. Gibson, and S. Aigrain, “Gaussian processes for time-series modelling,” *Philosophical Transactions of the Royal Society A: Mathematical, Physical and Engineering Sciences*, vol. 371, no. 1984, p. 20110550, 2013. [Online]. Available: <https://royalsocietypublishing.org/doi/abs/10.1098/rsta.2011.0550>
- [21] A. M. D. Livera, R. J. Hyndman, and R. D. Snyder, “Forecasting time series with complex seasonal patterns using exponential smoothing,” *Journal of the American Statistical Association*, vol. 106, no. 496, pp. 1513–1527, 2011. [Online]. Available: <https://doi.org/10.1198/jasa.2011.tm09771>
- [22] M. West and J. Harrison, *Bayesian forecasting and dynamic models*. Springer Science & Business Media, 2006.
- [23] P. R. Vlachas, W. Byeon, Z. Y. Wan, T. P. Sapsis, and P. Koumoutsakos, “Data-driven forecasting of high-dimensional chaotic systems with long short-term memory networks,” *Proceedings of the Royal Society A: Mathematical, Physical and Engineering Sciences*, vol. 474, no. 2213, p. 20170844, 2018.
- [24] R. J. Hyndman and G. Athanasopoulos, *Forecasting: principles and practice*. OTexts, 2018.
- [25] P. J. Schmid, “Dynamic mode decomposition of numerical and experimental data,” *Journal of Fluid Mechanics*, vol. 656, pp. 5–28, 2010.
- [26] Y.-T. Lin and H.-T. Wu, “ConceFT for Time-Varying Heart Rate Variability Analysis as a Measure of Noxious Stimulation During General Anesthesia,” *IEEE Transactions on Biomedical Engineering*, vol. 64, no. 1, pp. 145–154, 2017.
- [27] J. Alho and B. Spencer, *Statistical Demography and Forecasting*, ser. Springer Series in Statistics. Springer-Verlag New York, 2005.
- [28] L. Isserlis, “On a formula for the product-moment coefficient of any order of a normal frequency distribution in any number of variables,” *Biometrika*, vol. 12, no. 1-2, pp. 134–139, 11 1918. [Online]. Available: <https://doi.org/10.1093/biomet/12.1-2.134>
- [29] Y.-C. Chen, M.-Y. Cheng, and H.-T. Wu, “Non-parametric and adaptive modelling of dynamic periodicity and trend with heteroscedastic and dependent errors,” *Journal of the Royal Statistical Society Series B*, vol. 76, no. 3, pp. 651–682, June 2014. [Online]. Available: <https://ideas.repec.org/a/bla/jorssb/v76y2014i3p651-682.html>
- [30] I. Daubechies, Y. G. Wang, and H.-T. Wu, “ConceFT: concentration of frequency and time via a multitapered synchrosqueezed transform,” *Philosophical Transactions of the Royal Society A: Mathematical, Physical and Engineering Sciences*, vol. 374, no. 2065, p. 20150193, 2016. [Online]. Available: <https://royalsocietypublishing.org/doi/abs/10.1098/rsta.2015.0193>
- [31] M. Korda and I. Mezić, “Linear predictors for nonlinear dynamical systems: Koopman operator meets model predictive control,” *Automatica*, vol. 93, pp. 149 – 160, 2018. [Online]. Available: <http://www.sciencedirect.com/science/article/pii/S000510981830133X>
- [32] M. A. F. Pimentel, A. E. W. Johnson, P. H. Charlton, D. Birrenkott, P. J. Watkinson, L. Tarassenko, and D. A. Clifton, “Toward a robust estimation of respiratory rate from pulse oximeters,” *IEEE Transactions on Biomedical Engineering*, vol. 64, no. 8, pp. 1914–1923, 2017.
- [33] A. L. Goldberger, L. A. Amaral, L. Glass, J. M. Hausdorff, P. C. Ivanov, M. R. G., M. J. E., M. G. B., P. C. K., and S. H. E., “Physiobank, physiotoolkit, and physionet: Components of a new research resource for complex physiologic signals. circulation [online]. 101 (23),” *Circulation*, vol. 101, no. 23, pp. e215–e220, 2000.